ZnO Nanocones with High-Index {10ī1} Facets for Enhanced Energy Conversion Efficiency of Dye-Sensitized Solar Cells

7 AUTHORS, INCLUDING:

Jin Chang
The University of Electro-Communications
36 PUBLICATIONS **310** CITATIONS

SEE PROFILE

Hongxia Wang
Queensland University of Technology
53 PUBLICATIONS **1,023** CITATIONS

SEE PROFILE

Hongwei Liu
University of Sydney
124 PUBLICATIONS **2,296** CITATIONS

SEE PROFILE

Renzhi Li
Chinese Academy of Sciences
32 PUBLICATIONS **1,939** CITATIONS

SEE PROFILE

ZnO Nanocones with High-Index {10$\bar{1}$1} Facets for Enhanced Energy Conversion Efficiency of Dye-Sensitized Solar Cells

Jin Chang,[†] Rasin Ahmed,[†] Hongxia Wang,[†] Hongwei Liu,[‡] Renzhi Li,[§] Peng Wang,[§] and Eric R. Waclawik*,[†]

[†]School of Chemistry, Physics and Mechanical Engineering, Science and Engineering Faculty, Queensland University of Technology, Brisbane 4000, Australia

[‡]School of Materials Science and Engineering, Guangxi University, Nanning 530004, P. R. China

[§]State Key Laboratory of Polymer Physics and Chemistry, Changchun Institute of Applied Chemistry, Chinese Academy of Sciences, Changchun 130022, P. R. China

S *Supporting Information*

ABSTRACT: ZnO is a promising photoanode material for dye-sensitized solar cells (DSCs) due to its high bulk electron mobility and because different geometrical structures can easily be tailored. Although various strategies have been taken to improve ZnO-based DSC efficiencies, their performances are still far lower than TiO$_2$ counterparts, mainly because low conductivity Zn^{2+}−dye complexes form on the ZnO surfaces. Here, cone-shaped ZnO nanocrystals with exposed reactive O-terminated {10$\bar{1}$1} facets were synthesized and applied in DSC devices. The devices were compared with DSCs made from more commonly used rod-shaped ZnO nanocrystals where {10$\bar{1}$0} facets are predominantly exposed. When cone-shaped ZnO nanocrystals were used, DSCs sensitized with C218, N719, and D205 dyes universally displayed better power conversion efficiency, with the highest photoconversion efficiency of 4.36% observed with the C218 dye. First-principles calculations indicated that the enhanced DSCs performance with ZnO nanocone photoanodes could be attributed to the strength of binding between the dye molecules and reactive O-terminated {10$\bar{1}$1} ZnO facets and that more effective use of dye molecules occurred due to a significantly less dye aggregation on these ZnO surfaces compared to other ZnO facets.
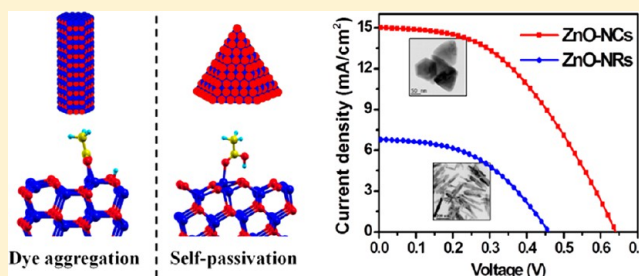
1. INTRODUCTION

Dye-sensitized solar cells (DSCs) have attracted extensive interest since the innovative work of O'Regan and Grätzel in 1991.[1] This field has grown fast because DSCs exhibited promising energy conversion efficiency, long-term stability, potentially low-cost production, and "plenty of room" to design on the nano or atomic scale.[2,3] The sandwich configuration of a DSC typically consists of a wide band gap semiconductor metal oxide film with adsorbed dye molecules as the photosensitized anode, an electrolyte containing I$^-$/I$_3^-$ redox couple as an electron/hole transporter, and a platinized fluorine-doped tin oxide (FTO) glass cathode. As the recipient of injected electrons from the photoexcited dye monolayer and also the conductive pathway, the photoanode is a significant factor that determines the power conversion efficiency (PCE). Since the breakthrough for DSCs in 1991, semiconductor metal oxides have been widely investigated as photoanode materials, with a record efficiency of 12.3% achieved for TiO$_2$-based DSCs.[3]

Although much research has been performed on TiO$_2$-based DSCs, ZnO is a promising alternative photoanode material that has attracted considerable attention recently due to its higher electron mobility (205−1000 cm^2 V^{-1} s^{-1}),[4] the similar energy level of its conduction band,[5] and its relative ease of synthesis compared to TiO$_2$. In fact, ZnO was one of the first metal oxides used as photoanode for the DSCs application. Recently, a variety of ZnO nanostructures, such as nanoparticles,[6,7] nanorods,[8] nanowire arrays,[9,10] and nanosheets,[11,12] have been tested, and the highest efficiency recorded to now is 7.5%, which is far lower than the conventional TiO$_2$-based DSCs.[13] Compared with TiO$_2$-based DSCs, the poor performance of ZnO photoanodes is mainly attributed to their lower chemical stability. The presence of carboxyl protons in commonly used dyes can etch ZnO surfaces during dye loading. For example, Chou et al. noted that the performance of DSCs is determined by the immersion time of ZnO electrodes in the dye solution and the dye concentration.[14] It was observed that the dissolution of ZnO by acidic carboxylic groups of dyes takes place at the crystal surface which leads to formation of Zn^{2+}−dye complexes that prevent the efficient injection of electrons.[15] Recent studies suggest that dyes with panchromatic absorption and lower acidity would be much better suited for ZnO-based DSCs.[16] On the other hand, weaker binding between dye and

ZnO might cause a weak and unstable sensitization, which has been noticed as bleaching in some DSCs.[17,18] In light of the complexity of the photovoltaic conversion process, a deeper understanding of ZnO-based DSCs is warranted, and a "better research focus" was strongly suggested to overcome the bottlenecks with conventional Grätzel cells.[19,20]

During the past two decades, various strategies have been taken to improve the photoconversion efficiencies of DSCs, mainly based on tailoring the morphology and crystal facets of metal oxide nanocrystals and a large amount of nanostructures have been tested as photoanodes. For example, TiO_2 nanocrystals with different percentages of exposed (001) facets were fabricated, and it was shown that nanocrystals with higher surface areas of exposed (001) facets are beneficial to DSC performance.[21−23] This is because atomic surface termination of semiconductors is highly relevant to their chemical reactivity[24] and electronic behavior.[25,26] The anatase (001) surfaces with high surface energy have strong ability to absorb dye molecules and therefore increase the electronic coupling between TiO_2 and dyes and favor the electron injection from excited state of dyes into the TiO_2 conduction band.[27] High-quality colloid nanocrystals can be synthesized in a variety of structural forms by controlling the kinetics of crystal growth in solution, usually by modifying nanocrystal surface energies through ligand effects.[28] The noncentrosymmetric crystal structure of wurtzite ZnO means that the shape of colloid crystallites as well as the crystal facet's chemistry and surface energy can be finely tuned and readily controlled. Although ZnO nanorods exposed with $\{10\bar{1}0\}$ facets have been widely used in DSCs, other morphologies with high-index facets have not. Therefore, in this work, ZnO nanocrystals with different shapes and therefore facet exposure were synthesized and used as photoanodes in DSCs. The surface termination of cone-shaped ZnO nanocrystals was determined by measuring a series of electron diffraction patterns. DSCs made from ZnO nanocrystals in the form of cones with exposed $\{10\bar{1}1\}$ facets were compared to rod-shaped samples in which $\{10\bar{1}0\}$ facets predominated at the crystal surfaces.

2. EXPERIMENTAL SECTION

2.1. Synthesis of ZnO Nanocrystals. The cone-shaped and rod-shaped ZnO nanocrystals were prepared using modified methods of our previous work.[29] For the synthesis of ZnO nanocones (ZnO-NCs), 0.92 g (5.0 mmol) of anhydrous zinc acetate ($Zn(OAc)_2$, Sigma-Aldrich), 0.77 g (2.0 mmol) of trioctylphosphine oxide (TOPO, Sigma-Aldrich), and 20 mL of benzyl ether (Sigma-Aldrich) were added into a 100 mL round-bottom flask. Then the mixture was stirred and heated at 120 °C for 1 h, followed by injection of 5.4 g (50 mmol) of benzylamine (Sigma-Aldrich) into the mixture. The reaction was continued for another 12 h at 180 °C. After cooling down to room temperature, the white precipitates were collected and washed three times with ethanol. The white powder was dried in an electric oven at 90 °C overnight. For the synthesis of ZnO nanorods (ZnO-NRs), 0.92 g (5.0 mmol) of $Zn(OAc)_2$, 0.77 g (2.0 mmol) of TOPO, and 20 mL of benzyl ether were mixed and heated to 220 °C. Then 0.54 g (5 mmol) of benzylamine was injected into the mixture and heated for another 5 h. After reaction, the white precipitates were collected and washed by ethanol, followed by drying in an electric oven at 90 °C overnight.

2.2. Characterization. The crystal structures of the prepared samples were identified by X-ray diffraction (XRD)

analysis using a PANanalytical XPert Pro Multi Purpose diffractometer (Cu $K\alpha$ radiation, λ = 0.154 178 nm). The morphologies of the materials were observed by field-emission scanning electron microscopy (FE-SEM, JEOL JSM-7001F) and transmission electron microscopy (TEM, JEOL JEM-2100). The serial electron diffraction patterns were obtained by a Philips/FEI CM12 microscope operated at 120 kV using a large angle double tilt holder. The specific surface area was estimated by the Brunauer−Emmett−Teller (BET) method based on the nitrogen adsorption/desorption isotherm with a micrometrics analyzer TriStar II 3020. Diffuse reflectance spectra were measured by a UV−vis−IR spectrometer (Varian, Cary 5000). X-ray photoelectron spectroscopy (XPS) spectra were measured by a Kratos Axis Ultra photoelectron spectrometer incorporating a 165 mm hemispherical electron-energy analyzer. All binding energies were referenced to the C 1s peak (284.6 eV) arising from adventitious carbon.

2.3. Fabrication of ZnO Films and Sensitization. ZnO pastes were prepared by mixing 0.2 g of ZnO powder sample (either ZnO-NCs or ZnO-NRs), 0.1 g of poly(ethylene glycol) (PEG, MW = 6000, Fluka), 0.05 g of hydroxypropyl cellulose (HPC, MW = 100 000, Acros Organics), and 0.8 g of deionized water. After stirring overnight, the resulting paste was doctor bladed onto the fluorine-doped tin oxide (FTO) conductive glass (TEC15, Hartford Glass). After evaporation of the solvent, the film was dried at 100 °C for 1 h and annealed at 400 °C for 30 min to remove the organic materials. The average thickness of one layer film was around 4.0 μm as determined by a stylus profilometer (Dektak 150). Then, the thickness of the film was increased by depositing a second layer of ZnO paste on top of the first one, followed by the same thermal treatment as for the first ZnO layer. The dye sensitization was performed by immersing the ZnO films in a 0.1 mM dye solution (C218, D205, or N719) in the mixture of acetonitrile and butanol (1:1 v/v) for 120 min. Coadsorbent of 1 mM chenodeoxycholic acid (Acros Organics) was added in the dye solution of C218 and D205 to reduce the dye aggregation on the ZnO films. The dye-loading amount in the ZnO film was determined by measuring the change of the concentration of the dye solution after the dye adsorption process by a UV−vis spectrometer (Varian, Cary 100).

2.4. Photovoltaic Performance of ZnO-Based DSCs. The dye-sensitized ZnO photoanode (active area: 0.25 cm^2) and the Pt counter electrode were assembled into a sandwich type cell. A drop of electrolyte solution containing 0.06 M I_2, 0.2 M NaI, 0.6 M 1-propyl-3-methylimidazolium iodide, and 0.5 M 4-*tert*-butylpyridine in 3-methoxypropionitrile was introduced into the gap between the two electrodes. The photocurrent density−voltage (J−V) characteristic curves of the solar cells were recorded with a computer-controlled digital source meter (Keithley 2306) by applying an external potential bias to the cell and measuring the photocurrent generated under a AM 1.5 solar simulator with an illumination density of 100 mW cm^{-2}. The J−V curves of the cells in darkness were also recoded to obtain the dark current.

2.5. Theoretical Calculations. *Ab initio* calculations were performed in the framework of density functional theory (DFT) methods by using the Quantum ESPRESSO package.[30] We used the Perdew, Burke, and Ernzerhof (PBE) gradient correction[31] and the ultrasoft Vanderbilt pseudopotentials.[32] Kohn−Sham eigenfunctions have been expanded on a plane-wave basis set using cutoffs of 30 Ry on the plane waves and 300 Ry on the electronic density. The bulk ZnO structure was
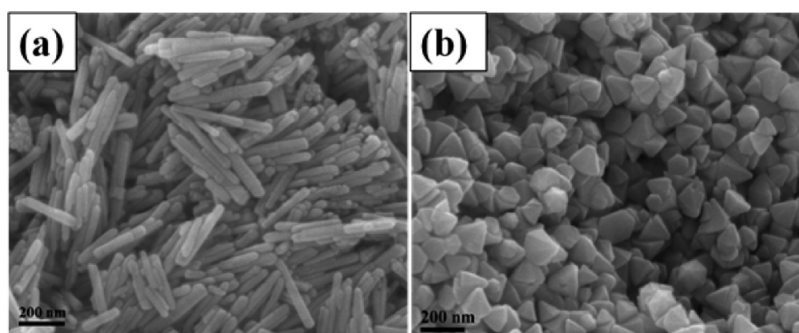
Figure 1. FE-SEM images of as-prepared (a) ZnO-NRs and (b) ZnO-NCs samples synthesized from zinc acetate and benzylamine using a hot-injection method.

first relaxed and the obtained a- and c-lattice parameters and μ are 3.287 Å, 5.301 Å, and 0.376, respectively, in good agreement with reported values.[33,34] For cleavage energy calculations, ZnO slabs with 1×1 lateral periodicity and different Zn−O bilayers (range from 2 to 10) were established. Slab replicas were separated by ∼20 Å of vacuum. Each structure was fully relaxed, and convergence was assumed when the forces on all atoms were lower than 0.001 eV/Å. To compare the dye adsorption on different ZnO surfaces, adsorbate geometries were optimized for each unit supercell of six atomic ZnO layers, with one acetic acid molecule on the surface. To verify that the neighboring adsorbate geometries were sufficiently isolated, vacuum thickness and surface size were increased until the change of adsorption energy was less than 0.01 eV. After the convergence test, 3×2 ($10\bar{1}0$) slabs and 2×3 ($10\bar{1}1$) slabs with ∼15 Å vacuum thickness were used for the calculation of adsorption energies. Different starting molecule−surface configurations have been considered and built up. The starting configurations were optimized by fully relaxing the positions of all atoms in a supercell, except for the atoms of the two bottom layers of ZnO slabs. All optimized geometries were plotted using the XCrySDen software.[35]

3. RESULTS AND DISCUSSION

3.1. Characterization. ZnO nanocrystals with different morphologies were prepared by a simple hot-injection method. Figure 1 shows the typical FE-SEM images of ZnO-NRs (a) and ZnO-NCs (b) nanocrystals, with rodlike and conelike morphologies, respectively. The XRD patterns shown in Figure S1 could be indexed to pure wurtzite ZnO crystal structures (JCPDS No. 36-1451). The relative intensity of (101) diffraction peak of ZnO-NCs was stronger than the corresponding peak of ZnO-NRs, presumably reflecting the fact that the $\{10\bar{1}1\}$ facet was preferentially exposed in the ZnO-NCs sample.

The TEM image in Figure 2a shows the rodlike morphology of ZnO-NRs with around 40 nm in width and 250 nm in length. The high-resolution transmission electron microscopy (HR-TEM) image of the ZnO-NRs shows a lattice spacing of 0.26 nm, which corresponds to the distance between $\{0002\}$ planes (Figure 2b). Figure 2c shows the selected area electron diffraction (SAED) pattern of the ZnO-NRs sample indicates that ZnO-NRs grow in the direction of [0001], which is the common growth direction of ZnO crystals. Figure 2d shows the TEM images of the ZnO-NCs, confirming their hexagonal conelike morphology with average size around 100 nm. As labeled in the image, the angle between the opposite edges at the tip of the cone is 64°, while the angles between edges and
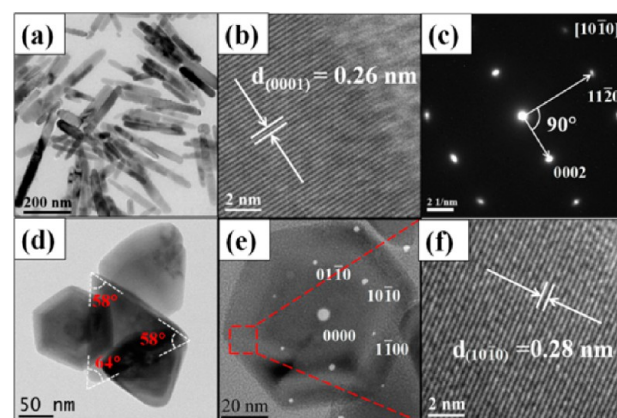

Figure 2. (a) TEM image of ZnO-NRs sample, (b) HR-TEM images of ZnO-NRs grown along [0001] direction, (c) the corresponding SAED pattern of ZnO-NRs, (d) TEM image of ZnO-NCs sample, (e) SAED pattern of one ZnO cone structure, and (f) the corresponding HR-TEM images of the marked area in (e).

the basal plane are 58°, which is consistent with the hexagonal cone structure model.[36] The SAED pattern of one single ZnO nanocone suggests that ZnO-NCs grow along the [0001] axis (Figure 2e). Although the growth direction was confirmed as [0001], the tip of the cone structure could point toward either [0001] or [000$\bar{1}$]. This was determined by measuring a series of electron diffraction patterns of the ZnO-NCs and was due to the noncentrosymmetric feature of the ZnO crystal structure. Considering the SAED pattern and the hexagonal cone structure, the exposed side surfaces were identified as $\{10\bar{1}1\}$ crystal facets. Figure 2f shows the HR-TEM image of the base facet of a ZnO cone as marked in Figure 2e. The image exhibits lattice fringes with spacing of 0.28 nm, which corresponds to the distance between $\{10\bar{1}0\}$ planes, and is consistent with the SAED characterization. Considering the similar dimensions of ZnO-NRs and ZnO-NCs samples, overall their surface areas were expected to be near-equal as well. This was confirmed when BET surface areas of ZnO-NCs and ZnO-NRs samples were determined from the nitrogen sorption isotherms and found to be 12.05 and 15.58 m^2 g^{-1}, respectively.

According to the above characterization, it was confirmed that ZnO-NCs possess a large percentage of exposed $\{10\bar{1}1\}$ facets, which was illustrated by the TEM images taken from different orientations (Figure 3a). As shown in Figure 3b, the ZnO ($10\bar{1}1$) slab model is always terminated with Zn and O ions on opposite sides of a slab. Therefore, the crystal surfaces of $\{10\bar{1}1\}$-faceted ZnO-NCs could either be Zn-terminated or
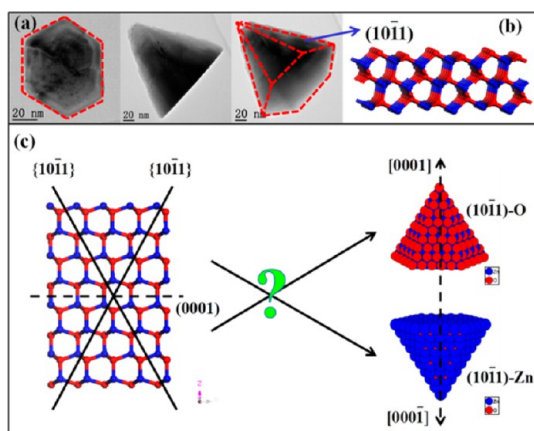
Figure 3. (a) TEM images of a conelike ZnO nanocrystal viewed from different orientations. (b) A slab model of ZnO (10$\bar{1}$1) surface. (c) Schematic illustration of conelike ZnO nanostructures with two termination possibilities, i.e., either Zn- or O-terminated, formed by cutting a crystal along {10$\bar{1}$1} planes. The blue and red spheres represent zinc and oxygen atoms, respectively.

O-terminated. Impressive work has been reported on ZnO double-cone structures, where Zn-terminated and O-terminated {10$\bar{1}$1} facets coexisted as shown by the surface contact potential images.[26] For the ZnO-NCs sample, the atomic termination of {10$\bar{1}$1} facets depends on the direction the tip of the ZnO-NCs points to. If the tip points toward the [0001]

direction, the cone structure will consist of six {10$\bar{1}$1}-O side surfaces and one {0001}-O base surface (Figure 3c). If the tip points toward [000$\bar{1}$] direction, the cone will consist of six {10$\bar{1}$1}-Zn side surfaces and one {0001}-Zn base surface. Although it has been proposed from the ZnO model that the conelike ZnO structure is O-surfaced,[36] it is actually not satisfactory to make this assumption because both models shown in Figure 3c are indistinguishable by either size or angle. Experimentally, conventional TEM characterization alone cannot identify the atomic termination because only an aberrated two-dimensional projection of the structure can be imaged. Recently, however, the termination of wurtzite rod-shaped ZnSe/ZnS core/shell structures were determined by aberration-corrected HR-TEM with exit wave reconstruction and aberration-corrected HAADF-STEM.[37] The termination of the crystal surface was well resolved even though this approach is often restricted by the sample size (especially the thickness), the special microscope instrument requirement, and advanced operation skills. In our work, the termination of ZnO-NCs was resolved by determining the growth direction of a single ZnO nanocone. By systematically tilting around a certain diffraction vector, the nonsingularity of 180° of the two-dimensional electron diffraction pattern could be established. Figure 4 shows a series of electron diffraction patterns taken of a single ZnO nanocone by systematic tilting. The indexing results indicated that the tip of the ZnO nanocone pointed to the [0001] direction, while the base plane faced to [000$\bar{1}$]. This can also be understood in terms of ZnO crystal structure. In a unit cell of a
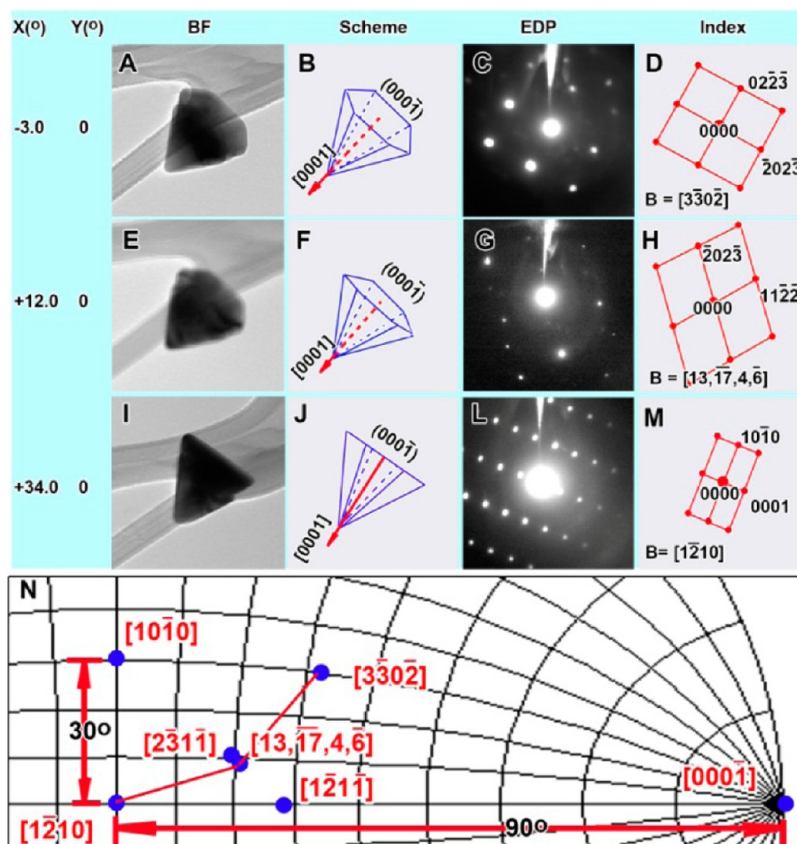
Figure 4. TEM investigation for the growth orientation of ZnO-NCs sample. Panels A, E, and I are TEM bright field images of a single ZnO nanocone; the corresponding schemes are shown in panel B, F, and J. The corresponding electron diffraction patterns (EDP) are shown in panels C, G, and L, with indexing result of EDP in panels D, H, and M. Part N is a section of stereographic projection with the pole center at [1$\bar{2}$10] of ZnO phase shows the tilting directions and the three experimental EDP directions.

hexagonal close-packed structure of ZnO, there are two Zn atoms and two O atoms. During the crystal growth, Zn atom clusters (growth building block) in the solvent environment are apt to bind with Zn atoms on (0001) plane but not $(000\bar{1})$ because of the higher atomic density at the former than the latter. As a result, ZnO-NCs tend to grow along the $[0001]$ direction but not the $[000\bar{1}]$ direction. It should be noted that for hexagonal structure $[uvtw]$ is parallel to the normal of plane $(uvtw)$; i.e., $[0001]$ is perpendicular to the plane (0001). Therefore, the basal plane could only be indexed as $(000\bar{1})$ in the electron diffraction pattern, and ZnO-NCs was determined to consist of six O-terminated $\{10\bar{1}1\}$ facets and one O-terminated $\{000\bar{1}\}$ facet.

3.2. Photovoltaic Measurements. To investigate the photovoltaic properties of the ZnO-NC and ZnO-NR samples, DSCs were fabricated and tested using the standard methods described in the experimental session. Figure 5 displays the
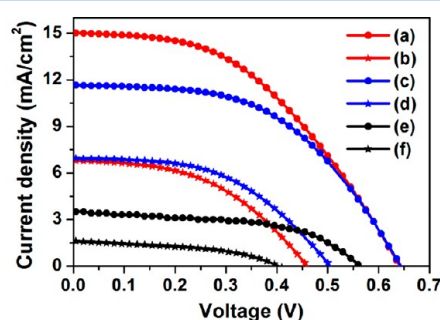
Figure 5. Comparison of the $J−V$ characteristics of the DSCs based on ZnO-NCs and ZnO-NRs with different dyes: (a) C218/ZnO-NCs, (b) C218/ZnO-NRs, (c) N719/ZnO-NCs, (d) N719/ZnO-NRs, (e) D205/ZnO-NCs, and (f) D205/ZnO-NRs.

photocurrent−voltage $(J−V)$ characteristics of the DSCs fabricated from ZnO films based on ZnO-NCs and ZnO-NRs sensitized with three different dyes C218, N719, and D205 (the dye molecular structures are given in Figure S2). Three identical cells were made for each type of DSC to ensure reproducible results. The characteristic photovoltaic parameters of these cells and the dye loading of the ZnO films are summarized in Table 1. By comparing the $J−V$ curves of these DSCs, it is clear that, irrespective of the different sensitizing dye type, the ZnO-NC-based DSCs always exhibited better performance than those of ZnO-NRs. The C218-sensitized ZnO-NCs cell (C218/ZnO-NCs) exhibited the highest efficiency (η = 4.36%), which is 3 times the efficiency of C218/ZnO-NRs cell (η = 1.45%). Similarly, the efficiencies of N719/ZnO-NCs and D205/ZnO-NCs cells are nearly twice the value of the corresponding ZnO-NRs cells. The higher

efficiency of ZnO-NCs-based cell is attributed to the much higher short-circuit current density (J_{sc}) and open-circuit voltage (V_{oc}). The J_{sc} of ZnO-NCs-based DSCs is always around twice the value of the corresponding ZnO-NRs cells. This indicates the ZnO-NCs with $\{10\bar{1}1\}$ facets exposed lead to enhanced DSC performance compared to the ZnO-NRs with exposed $\{10\bar{1}0\}$ facets.

The J_{sc} of a DSC depends on many factors, including the light harvesting efficiency, the electron injection efficiency, and the electron collection efficiency.[38] Considering that ZnO-NCs have lower surface areas with lower dye loading than ZnO-NRs (with the exception of the N719-sensitized DSCs, where dye loading is comparable to ZnO-NR DSCs) and the dimensions of ZnO-NCs were comparable to ZnO-NRs, a lower light harvesting efficiency is expected for the ZnO-NCs cells compared to the ZnO-NRs cells. Therefore, the higher J_{sc} of the ZnO-NCs-based cells is likely to be due to the preponderance of the exposed reactive $\{10\bar{1}1\}$ facets, which must engender improved electron injection and/or electron collection process in the device. For ZnO-based DSCs, dye aggregation issue often causes inefficient electron injection.[20] The higher dye loading in the ZnO-NRs based films suggests that the aggregation issue of dye molecule on the surface of ZnO-NRs is likely to be more serious than on ZnO-NC surfaces. This can be rationalized by considering the surface atomic termination of the ZnO crystals. The effect of surface termination of ZnO-NRs and ZnO-NCs on the dye adsorption is illustrated in Figure 6. Apparently, exposed reactive Zn^{2+} sites interact with the dye molecules to form Zn^{2+}−dye complexes on the surface of ZnO-NRs that hinders effective charge separation and therefore reduces the electron injection from the dye excited state to the conduction band of ZnO-NRs. In contrast, ZnO-NCs with the O-terminated crystal facets prevent the formation of these Zn^{2+}−dye complexes. This can be considered a self-passivation effect during the dye-uptake procedure that reduces dye aggregation, and so the final photoanode is more efficient in terms of electron injection compared to the Zn-terminated ZnO-NRs. Similar consideration about the effect of surface termination on dye uptake of ZnO has been investigated by near-edge X-ray absorption fine structure (NEXAFS) spectroscopy.[39] It was observed that an interface reaction took place where the hydrogen in dye H₂-protoporphyrin could be substituted by a Zn atom from the nonpolar ZnO $(10\bar{1}0)$ surface, which supports our understanding for ZnO-NRs. Although the O-terminated ZnO-NCs are relatively stable in the acidic medium in DSCs, the nature of the dye molecule also has significant influence on the stability of our systems because it is unlikely that the synthesized ZnO-NCs are all uniformly perfect in shape. It is likely that trace amounts of Zn^{2+} ions could be exposed at the surface to contact

Table 1. Comparison of the Characteristic $J−V$ Parameters and Dye Loadings of the DSCs Based on ZnO-NCs and ZnO-NRs Sensitised with Different Dyes[a]

cells	J_{sc} (mA/cm²)	V_{oc} (mV)	FF	η (%)	dye loading (10^{-4} mol/cm³)
C218/ZnO-NCs	15.0	639	0.45	4.36 ± 0.4	0.790
C218/ZnO-NRs	6.80	462	0.46	1.45 ± 0.07	1.32
N719/ZnO-NCs	11.6	647	0.50	3.84 ± 0.2	1.49
N719/ZnO-NRs	6.93	505	0.49	1.73 ± 0.2	1.46
D205/ZnO-NCs	3.51	548	0.54	1.04 ± 0.3	0.360
D205/ZnO-NRs	1.62	385	0.47	0.380 ± 0.2	1.79

[a]$J−V$ measurements were performed under AM 1.5 solar spectra with light intensity of 100 mW cm^{-2} (cell active areas 0.25 cm²).
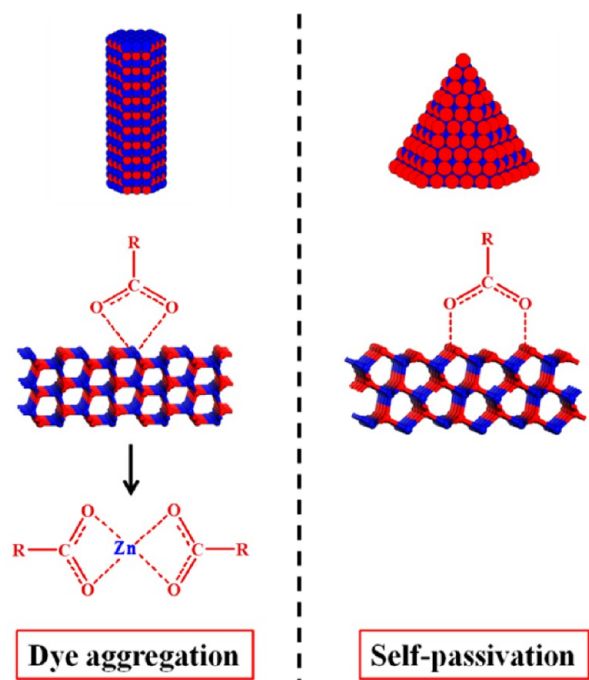
Figure 6. Illustration of the surface termination effects of ZnO on dye adsorption of DSCs. Left: the nonpolar $(10\bar{1}0)$ surface of ZnO-NRs, which contains an equal number of O and Zn ions, can be etched by acidic dye molecules, resulting in dye aggregation. Right: the adsorption of dye on the O-terminated $(10\bar{1}1)$ surface of ZnO-NCs, which is self-passivated owing to the protective effect of oxygen atoms to the reactive Zn^{2+} sites.

with dye molecules, which lead to the formation of the unwanted Zn^{2+}–dye complexes. This aside, using dye molecules with less carboxyl groups (e.g., C218) rather than dyes with multiple carboxyl groups (e.g., N719) can improve the stability of ZnO-based DSCs.

It is known that V_{oc} of a DSC is determined by the difference between the Fermi level of the semiconductor (e.g., ZnO) of the photoanode and the redox potential of I^-/I_3^- in the electrolyte. The Fermi level of the semiconductor depends on its conduction band edge (E_{cb}) and the electron density. The conduction band edges of the ZnO-NCs and ZnO-NRs were estimated by UV–vis spectra combined with valence-band (VB) X-ray photoelectron spectra (XPS). UV–vis spectra (Figure 7a) indicated that the band gaps of ZnO-NCs and ZnO-NRs were 3.21 and 3.15 eV, respectively. The valence-band XPS (Figure 7b) revealed that the valence band maximum of both ZnO nanostructures was 3.08 eV, which is consistent with reported values.[40] Therefore, the E_{cb} of ZnO-NCs is more

negative compared to that of the ZnO-NRs. Moreover, it has been reported that the E_{cb} of a semiconductor is also affected by dye adsorption. E_{cb} tends to shift positively due to the protonation of the semiconductor surface by adsorbed dye molecules.[41] Hence, the E_{cb} of ZnO-NRs could be dragged down further compared to that of the ZnO-NCs because of the higher dye loading. The higher E_{cb} of ZnO-NCs is beneficial in leading to a higher V_{oc} of the DSC. However, it reduces the driving force for electron injection from the excited state of the dye molecule to ZnO, which may lead to the decrease of J_{sc} of the device. Nevertheless, the absence of Zn^{2+}–dye complexes on the O-terminated ZnO-NCs nanocrystals could significantly benefit the electron injection compared to the ZnO-NRs/dye, where far larger quantities of the unwanted Zn^{2+}–dye complexes are present at the crystal surface. The higher J_{sc} of ZnO-NCs-based DSC suggests that the benefits of O-terminated surfaces in ZnO-NCs, which prevents the formation of Zn^{2+}–dye complexes in the photoanode, surpasses any deleterious effect of the higher E_{cb} in terms of electron injection in the DSC. Figure 7c illustrates the working principle of ZnO-based DSCs and the different conduction band energy level of ZnO-NCs and ZnO-NRs photoanode.

It is known that recombination at the interfaces of both the photoanode/electrolyte and FTO/electrolyte can result in a loss of photocurrent.[42] Therefore, dark current measurements were performed to obtain an estimation of electron recombination in the DSCs. As shown in Figure 8, the dark
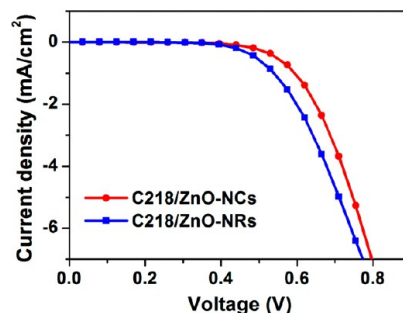
Figure 8. Dark current–voltage characteristics of C218/ZnO-NCs and C218/ZnO-NRs DSCs.

current onset of the C218/ZnO-NRs cell shifted to a slightly lower potential than the C218/ZnO-NCs cell and generated a smaller dark current at the potentials above 0.4 V. These observations reflect a lower charge recombination between electrons and I_3^- ions for photoanodes fabricated with ZnO-NCs. The porous structure of the photoanode permits electrolyte species such as I_3^- to infiltrate the film and contact
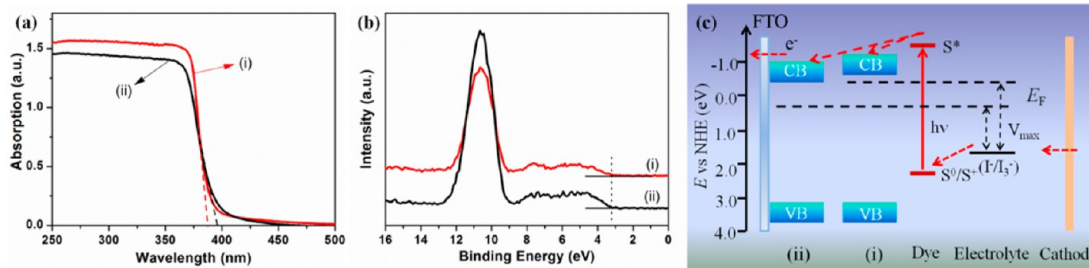

Figure 7. (a) UV–vis absorption spectra. (b) XPS valence band spectra. (c) Schematic of DSCs using either (i) ZnO-NCs or (ii) ZnO-NRs as a photoanode, where ZnO-NCs cell exhibits higher V_{max} value caused by the upshift of the conduction band energy level.

the FTO surface. It is unlikely that the origin of the observed differences in recombination is due to the minor differences in crystallinity or particle size of the ZnO-NCs and ZnO-NRs, since the syntheses were essentially the same and the product particle sizes were similar. The observed differences in the DSCs dark current more likely arose from a difference in the interfacial recombination at dye-coated ZnO-NCs/electrolyte compared to ZnO-NRs/electrolyte.

3.3. Computational Simulation. To better understand the ZnO-NCs and ZnO-NRs samples, a series of first-principle calculations were performed on the surface energies and molecule absorption energies of both ZnO types using the Quantum-ESPRESSO package. The surface energies of nonpolar $(10\bar{1}0)$ ZnO surfaces can be obtained from slab calculations, while this is not possible for the polar (0001) and $(10\bar{1}1)$ surfaces since both Zn and O terminations are present in a slab calculation. Therefore, cleavage energies of ZnO surfaces were calculated to compare the relative stability of the nonpolar and polar surfaces. The cleavage energies of ZnO surfaces as a function of slab thickness are shown in Figure 9. As expected, the high-index polar $(10\bar{1}1)$ surface is
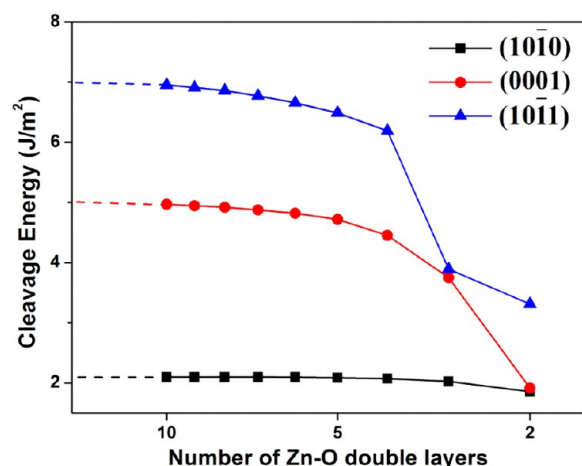
Figure 9. Cleavage energies of ZnO surfaces calculated with different slabs containing various Zn−O bilayers and using the PBE functional.

the most unstable facet of ZnO, with the highest cleavage energy of around 7.0 J/m². The nonpolar $(10\bar{1}0)$ surface is the most stable ZnO facet with the lowest cleavage energy of 2.1 J/m². The (0001)-O surface corresponding to the base facet of ZnO-NCs has moderate stability and reactivity. This is consistent with experimental results that ZnO tends to be formed with the exposure of low surface energy $(10\bar{1}0)$ facets. In contrast, ZnO exposed with high surface energy $(10\bar{1}1)$ facets are reactive in the solution environment and can only be prepared with the assistance of capping molecules.

To investigate the different adsorption modes of an acid on ZnO surfaces, adsorbate geometries were optimized for 3 × 2 $(10\bar{1}0)$ slabs and 2 × 3 $(10\bar{1}1)$ slabs, with acetic acid on the surfaces. The adsorption energy, E_{ads}, is calculated using the equation

$$E_{ads} = E_{slab} + E_{acid} - E_{slab+acid}$$

where E_{slab} represents the energy of the clean slab, E_{acid} is the energy of the adsorbate, and $E_{slab+acid}$ is the total energy of the slab with adsorbate.

According to the anchoring mechanism of the carboxyl group (COO^-) to metal ions,[43] there are three possible adsorption modes of carboxylic acid groups on ZnO surfaces: monodentate, bidentate chelating, and bidentate bridging (Figure 10). Adsorption geometries with acetic acid molecules on ZnO
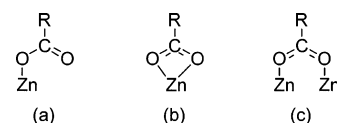
Figure 10. Three possible adsorption modes of carboxylic acid group on ZnO surfaces: (a) monodentate, (b) bidentate chelating, and (c) bidentate bridging.

$(10\bar{1}0)$ surfaces were optimized from different starting configurations. Figure 11 shows the optimized geometries
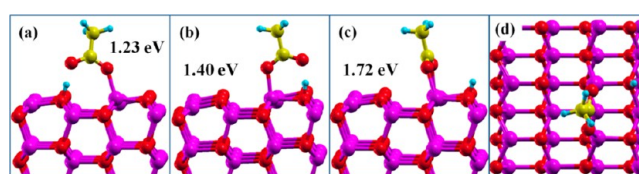
Figure 11. Side views of the optimized adsorption geometries and corresponding adsorption energies of acetic acid on ZnO $(10\bar{1}0)$ surface: (a) monodentate 1 (M1), (b) monodentate 2 (M2), and (c) bidentate bridging (BB). (d) Top view of the optimized geometry of BB configuration. Zn, O, C, and H atoms are represented by purple, red, yellow, and green spheres, respectively.

and the corresponding adsorption energies of acetic acid on ZnO $(10\bar{1}0)$ surface. It was observed that the optimized configurations were either monodentate (M1, M2) mode or bidentate bridging (BB) mode. The proposed bidentate chelating structure was not observed in this system, which was consistent with other reported dye adsorption simulations.[44] For all optimized geometries, the acetic acid molecule was dissociated, with the proton transferred to nearby oxygen atoms on ZnO surface. Among these geometries, the most favorable configuration was the BB mode, with two carboxyl oxygen atoms bound to two zinc atoms of ZnO (Figure 11c). The adsorption energies of M1, M2, and BB modes are 1.23, 1.40, and 1.72 eV, respectively.

For the O-terminated ZnO $(10\bar{1}1)$ surface, zinc atoms in the second layer moved toward the surface and interacted with one carboxyl oxygen atom of the acetic acid. During the relaxation path, the acetic acid was either dissociated to release a H^+ ion from the carboxyl group or undissociated with the H atom approached to neighboring O atoms of ZnO surface (Figure 12). All optimized adsorption geometries of acetic acid on ZnO
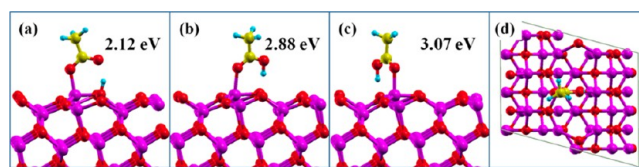
Figure 12. Side views of the optimized adsorption geometries and corresponding adsorption energies of acetic acid on ZnO $(10\bar{1}1)$ surface: (a) dissociative mode; (b, c) undissociative mode. (d) Top view of the optimized geometry of the 2 × 3 ZnO slab with acetic acid on the $(10\bar{1}1)$ surface.

($10\bar{1}1$) surfaces were monodentate, with one carboxyl oxygen atom bound to one zinc atom of ZnO. The most energetically favorable geometry was undissociative mode, with the adsorption energy of 3.07 eV (Figure 12c). From comparison of the simulations illustrated in Figures 11 and 12, the adsorption energies of acetic acid on ZnO ($10\bar{1}1$) surfaces were much higher than those on the ($10\bar{1}0$) surface. The most favorable adsorption mode was monodentate with undissociated molecule on ($10\bar{1}1$) surfaces, while bidentate bridging mode with dissociated molecule on ($10\bar{1}0$) surface. This means the Zn and O atoms on a ($10\bar{1}0$) surface are more likely to be etched by carboxyl oxygen atoms and dissociated protons of dye molecules, resulting into the formation of unwanted $Zn^{2+}-$dye complexes, i.e., dye aggregation. In the case of O-terminated ($10\bar{1}1$) surface, molecules should remain undissociated, and the ZnO surface is therefore passivated by O atoms, leading to more efficient use of dye molecules in the DSC photoanodes, without the formation of $Zn^{2+}-$dye complexes.

4. CONCLUSIONS

In summary, single-crystalline ZnO-NCs and ZnO-NRs were selectively prepared by a hot-injection method with either mainly exposed {$10\bar{1}1$} or {$10\bar{1}0$} facets, respectively. The surface atomic termination of ZnO-NCs was determined by measuring the serial electron diffraction patterns of a single ZnO nanocone. The DSC assembled with C218 dye-coated ZnO-NCs photoanodes demonstrated the highest overall conversion efficiency of 4.36%, which was 3 times the efficiency obtained from the ZnO-NRs counterpart. This result is remarkable, especially when taking into account the relatively low surface area of the ZnO nanocrystals. Similar efficiency improvement with the ZnO-NCs photoanodes compared to ZnO-NRs was also found in the case of another two dyes (N719 and D205). Compared to ZnO-NRs-based DSCc, the over 2-fold enhancement in J_{sc} and over 150 mV increase in V_{oc} of the ZnO-NCs-based DSCs were ascribed to the beneficial effect of the reactive high-index {$10\bar{1}1$} facets with O termination. This work suggests the possibility of achieving higher photoconversion efficiency in ZnO-based DSCs by taking advantage of the active ZnO {$10\bar{1}1$} facets to control the dye aggregation on the surface of ZnO material.

■ ASSOCIATED CONTENT

Ⓢ Supporting Information

XRD patterns and dye molecular structures. This material is available free of charge via the Internet at http://pubs.acs.org.

■ AUTHOR INFORMATION

Corresponding Author

*Fax +61 7 3138 1804; Tel +61 7 3138 2579; e-mail e. waclawik@qut.edu.au (E.R.W.).

Notes

The authors declare no competing financial interest.

■ ACKNOWLEDGMENTS

■ REFERENCES

(1) Oregan, B.; Gratzel, M. A Low-Cost, High-Efficiency Solar Cell Based on Dye-Sensitized Colloidal TiO₂ Films. *Nature* **1991**, *353*, 737−740.

(2) Sun, P.; Zhang, X.; Wang, C.; Wei, Y.; Wang, L.; Liu, Y. Rutile TiO₂ Nanowire Array Infiltrated with Anatase Nanoparticles as Photoanode for Dye-Sensitized Solar Cells: Enhanced Cell Performance via the Rutile-Anatase Heterojunction. *J. Mater. Chem. A* **2013**, *1*, 3309−3314.

(3) Yella, A.; Lee, H.-W.; Tsao, H. N.; Yi, C.; Chandiran, A. K.; Nazeeruddin, M. K.; Diau, E. W.-G.; Yeh, C.-Y.; Zakeeruddin, S. M.; Grätzel, M. Porphyrin-Sensitized Solar Cells with Cobalt (II/III)-Based Redox Electrolyte Exceed 12% Efficiency. *Science* **2011**, *334*, 629−634.

(4) Zhang, Q.; Dandeneau, C. S.; Zhou, X.; Cao, G. ZnO Nanostructures for Dye-Sensitized Solar Cells. *Adv. Mater.* **2009**, *21*, 4087−4108.

(5) Katoh, R.; Furube, A.; Yoshihara, T.; Hara, K.; Fujihashi, G.; Takano, S.; Murata, S.; Arakawa, H.; Tachiya, M. Efficiencies of Electron Injection from Excited N3 Dye into Nanocrystalline Semiconductor (ZrO₂, TiO₂, ZnO, Nb₂O₅, SnO₂, In₂O₃) Films. *J. Phys. Chem. B* **2004**, *108*, 4818−4822.

(6) Marczak, R.; Werner, F.; Ahmad, R.; Lobaz, V.; Guldi, D. M.; Peukert, W. Detailed Investigations of ZnO Photoelectrodes Preparation for Dye Sensitized Solar Cells. *Langmuir* **2011**, *27*, 3920−3929.

(7) Zhang, Q.; Chou, T. P.; Russo, B.; Jenekhe, S. A.; Cao, G. Aggregation of ZnO Nanocrystallites for High Conversion Efficiency in Dye-Sensitized Solar Cells. *Angew. Chem., Int. Ed.* **2008**, *47*, 2402−2406.

(8) Zheng, Y.-Z.; Zhao, J.; Zhang, H.; Chen, J.-F.; Zhou, W.; Tao, X. Dual-Functional ZnO Nanorod Aggregates as Scattering Layer in the Photoanode for Dye-Sensitized Solar Cells. *Chem. Commun.* **2011**, *47*, 11519−11521.

(9) Law, M.; Greene, L. E.; Johnson, J. C.; Saykally, R.; Yang, P. D. Nanowire Dye-Sensitized Solar Cells. *Nat. Mater.* **2005**, *4*, 455−459.

(10) Wang, M.; Wang, Y.; Li, J. ZnO Nanowire Arrays Coating on TiO₂ Nanoparticles as a Composite Photoanode for a High Efficiency DSSC. *Chem. Commun.* **2011**, *47*, 11246−11248.

(11) Lin, C.-Y.; Lai, Y.-H.; Chen, H.-W.; Chen, J.-G.; Kung, C.-W.; Vittal, R.; Ho, K.-C. Highly Efficient Dye-Sensitized Solar Cell with a ZnO Nanosheet-Based Photoanode. *Energy Environ. Sci.* **2011**, *4*, 3448−3455.

(12) Kung, C.-W.; Chen, H.-W.; Lin, C.-Y.; Lai, Y.-H.; Vittal, R.; Ho, K.-C. Electrochemical Synthesis of a Double-Layer Film of ZnO Nanosheets/Nanoparticles and Its Application for Dye-Sensitized Solar Cells. *Prog. Photovoltaics* **2012**, DOI: 10.1002/pip.2288.

(13) Memarian, N.; Concina, I.; Braga, A.; Rozati, S. M.; Vomiero, A.; Sberveglieri, G. Hierarchically Assembled ZnO Nanocrystallites for High-Efficiency Dye-Sensitized Solar Cells. *Angew. Chem., Int. Ed.* **2011**, *50*, 12321−12325.

(14) Chou, T. P.; Zhang, Q.; Cao, G. Effects of Dye Loading Conditions on the Energy Conversion Efficiency of ZnO and TiO₂ Dye-Sensitized Solar Cells. *J. Phys. Chem. C* **2007**, *111*, 18804−18811.

(15) Katoh, R.; Furube, A.; Tamaki, Y.; Yoshihara, T.; Murai, M.; Hara, K.; Murata, S.; Arakawa, H.; Tachiya, M. Microscopic Imaging of the Efficiency of Electron Injection from Excited Sensitizer Dye into Nanocrystalline ZnO Film. *J. Photochem. Photobiol., A* **2004**, *166*, 69−74.

(16) Guillén, E.; Casanueva, F.; Anta, J. A.; Vega-Poot, A.; Oskam, G.; Alcántara, R.; Fernández-Lorenzo, C.; Martín-Calleja, J. Photovoltaic Performance of Nanostructured Zinc Oxide Sensitised with Xanthene Dyes. *J. Photochem. Photobiol., A* **2008**, *200*, 364−370.

(17) Le Bahers, T.; Labat, F.; Pauporte, T.; Ciofini, I. Effect of Solvent and Additives on the Open-Circuit Voltage of ZnO-based Dye-Sensitized Solar Cells: A Combined Theoretical and Experimental Study. *Phys. Chem. Chem. Phys.* **2010**, *12*, 14710−14719.

(18) Guillen, E.; Idigoras, J.; Berger, T.; Anta, J. A.; Fernandez-Lorenzo, C.; Alcantara, R.; Navas, J.; Martin-Calleja, J. ZnO-based Dye

13843

dx.doi.org/10.1021/jp402742n | *J. Phys. Chem. C* 2013, 117, 13836−13844

Solar Cell with Pure Ionic-liquid Electrolyte and Organic Sensitizer: the Relevance of the Dye-Oxide Interaction in an Ionic-Liquid Medium. *Phys. Chem. Chem. Phys.* **2011**, *13*, 207−213.

(19) Peter, L. M. The Grätzel Cell: Where Next? *J. Phys. Chem. Lett.* **2011**, *2*, 1861−1867.

(20) Anta, J. A.; Guillén, E.; Tena-Zaera, R. ZnO-Based Dye-Sensitized Solar Cells. *J. Phys. Chem. C* **2012**, *116*, 11413−44425.

(21) Wu, X.; Chen, Z.; Lu, G. Q.; Wang, L. Nanosized Anatase TiO_2 Single Crystals with Tunable Exposed (001) Facets for Enhanced Energy Conversion Efficiency of Dye-Sensitized Solar Cells. *Adv. Funct. Mater.* **2011**, *21*, 4167−4172.

(22) Yu, J.; Fan, J.; Lv, K. Anatase TiO_2 Nanosheets with Exposed (001) Facets: Improved Photoelectric Conversion Efficiency in Dye-Sensitized Solar Cells. *Nanoscale* **2010**, *2*, 2144−2149.

(23) Wang, H. X.; Liu, M. N.; Yan, C.; Bell, J. Reduced Electron Recombination of Dye-Sensitized Solar Cells Based on TiO_2 Spheres Consisting of Ultrathin Nanosheets with (001) Facet Exposed. *Beilstein J. Nanotechnol.* **2012**, *3*, 378−387.

(24) Rempel, J. Y.; Trout, B. L.; Bawendi, M. G.; Jensen, K. F. Properties of the CdSe(0001), (000−1), and (11−20) Single Crystal Surfaces: Relaxation, Reconstruction, and Adatom and Admolecule Adsorption. *J. Phys. Chem. B* **2005**, *109*, 19320−19328.

(25) Brillson, L. J.; Lu, Y. C. ZnO Schottky Barriers and Ohmic Contacts. *J. Appl. Phys.* **2011**, *109*, 121301−121333.

(26) Zúñiga-Pérez, J.; Muñoz-Sanjosé, V.; Palacios-Lidón, E.; Colchero, J. Polarity Effects on ZnO Films Grown along the Nonpolar [11−20] Direction. *Phys. Rev. Lett.* **2005**, *95*, 226105.

(27) Yang, W.; Li, J.; Wang, Y.; Zhu, F.; Shi, W.; Wan, F.; Xu, D. A Facile Synthesis of Anatase TiO_2 Nanosheets-Based Hierarchical Spheres with over 90% {001} Facets for Dye-Sensitized Solar Cells. *Chem. Commun.* **2011**, *47*, 1809−1811.

(28) Manna, L.; Scher, E. C.; Alivisatos, A. P. Synthesis of Soluble and Processable Rod-, Arrow-, Teardrop-, and Tetrapod-Shaped CdSe Nanocrystals. *J. Am. Chem. Soc.* **2000**, *122*, 12700−12706.

(29) Chang, J.; Waclawik, E. R. Facet-Controlled Self-Assembly of ZnO Nanocrystals by Non-hydrolytic Aminolysis and Their Photodegradation Activities. *CrystEngComm* **2012**, *14*, 4041−4048.

(30) Paolo, G.; Stefano, B.; Nicola, B.; Matteo, C.; Roberto, C.; Carlo, C.; Davide, C.; Guido, L. C.; Matteo, C.; Ismaila, D.; et al. Quantum ESPRESSO: a Modular and Open-Source Software Project for Quantum Simulations of Materials. *J. Phys.: Condens. Matter* **2009**, *21*, 395502.

(31) Perdew, J. P.; Burke, K.; Ernzerhof, M. Generalized Gradient Approximation Made Simple. *Phys. Rev. Lett.* **1996**, *77*, 3865−3868.

(32) Vanderbilt, D. Soft Self-Consistent Pseudopotentials in a Generalized Eigenvalue Formalism. *Phys. Rev. B* **1990**, *41*, 7892−7895.

(33) Calzolari, A.; Ruini, A.; Catellani, A. Anchor Group versus Conjugation: Toward the Gap-State Engineering of Functionalized ZnO(10−10) Surface for Optoelectronic Applications. *J. Am. Chem. Soc.* **2011**, *133*, 5893−5899.

(34) Meyer, B.; Marx, D. Density-Functional Study of the Structure and Stability of ZnO Surfaces. *Phys. Rev. B* **2003**, *67*, 035403.

(35) Kokalj, A. Computer Graphics and Graphical User Interfaces as Tools in Simulations of Matter at the Atomic Scale. *Comput. Mater. Sci.* **2003**, *28*, 155−168.

(36) Zhou, X.; Xie, Z.-X.; Jiang, Z.-Y.; Kuang, Q.; Zhang, S.-H.; Xu, T.; Huang, R.-B.; Zheng, L.-S. Formation of ZnO Hexagonal Micro-Pyramids: a Successful Control of the Exposed Polar Surfaces with the Assistance of an Ionic Liquid. *Chem. Commun.* **2005**, 5572−5574.

(37) Bertoni, G.; Grillo, V.; Brescia, R.; Ke, X.; Bals, S.; Catellani, A.; Li, H.; Manna, L. Direct Determination of Polarity, Faceting, and Core Location in Colloidal Core/Shell Wurtzite Semiconductor Nanocrystals. *ACS Nano* **2012**, *6*, 6453−6461.

(38) Wang, H.; Peter, L. M. A Comparison of Different Methods to Determine the Electron Diffusion Length in Dye-Sensitized Solar Cells. *J. Phys. Chem. C* **2009**, *113*, 18125−18133.

(39) González-Moreno, R.; Cook, P. L.; Zegkinoglou, I.; Liu, X.; Johnson, P. S.; Yang, W.; Ruther, R. E.; Hamers, R. J.; Tena-Zaera, R.; Himpsel, F. J.; et al. Attachment of Protoporphyrin Dyes to Nanostructured ZnO Surfaces: Characterization by Near Edge X-ray Absorption Fine Structure Spectroscopy. *J. Phys. Chem. C* **2011**, *115*, 18195−18201.

(40) Kim, T.; Yoshitake, M.; Yagyu, S.; Nemsak, S.; Nagata, T.; Chikyow, T. XPS Study on Band Alignment at Pt-O-terminated ZnO(0001) Interface. *Surf. Interface Anal.* **2010**, *42*, 1528−1531.

(41) Wang, H.; Liu, M.; Zhang, M.; Wang, P.; Miura, H.; Cheng, Y.; Bell, J. Kinetics of Electron Recombination of Dye-sensitized Solar Cells Based on TiO_2 Nanorod Arrays Sensitized with Different Dyes. *Phys. Chem. Chem. Phys.* **2011**, *13*, 17359−17366.

(42) Ito, S.; Liska, P.; Comte, P.; Charvet, R.; Pechy, P.; Bach, U.; Schmidt-Mende, L.; Zakeeruddin, S. M.; Kay, A.; Nazeeruddin, M. K.; et al. Control of Dark Current in Photoelectrochemical (TiO_2/I^--I_3^-) and Dye-Sensitized Solar Cells. *Chem. Commun.* **2005**, 4351−4353.

(43) Nara, M.; Torii, H.; Tasumi, M. Correlation between the Vibrational Frequencies of the Carboxylate Group and the Types of Its Coordination to a Metal Ion: An ab Initio Molecular Orbital Study. *J. Phys. Chem.* **1996**, *100*, 19812−19817.

(44) Srinivas, K.; Yesudas, K.; Bhanuprakash, K.; Rao, V. J.; Giribabu, L. A Combined Experimental and Computational Investigation of Anthracene Based Sensitizers for DSSC: Comparison of Cyanoacrylic and Malonic Acid Electron Withdrawing Groups Binding onto the TiO_2 Anatase (101) Surface. *J. Phys. Chem. C* **2009**, *113*, 20117−20126.